Ionic Hydrogen Bond-Assisted Catalytic Construction of Nitrogen Stereogenic Center via Formal Desymmetrization of Remote Diols

Zhongfu Luo,[a] Minghong Liao,[a] Wei Li,[a] Sha Zhao,[a] Kun Tang,[a] Pengcheng Zheng,[a] Yonggui Robin Chi[a][b], Xinglong Zhang*[c] and Xingxing Wu*[a]

[a] National Key Laboratory of Green Pesticide, Key Laboratory of Green Pesticide and Agricultural Bioengineering, Ministry of Education, Guizhou University, Huaxi District, Guiyang 550025, China.
[b] School of chemistry, chemical engineering, and biotechnology, Nanyang Technological University, Singapore 637371, Singapore
[c] Institute of High Performance Computing (IHPC), Agency for Science, Technology and Research (A*STAR), Singapore 138632, Singapore.
*Correspondence:
E-mail: wuxx@gzu.edu.cn, zhang_xinglong@ihpc.a-star.edu.sg

4. Computational section

4.1 Model reaction

Due to the high computational cost, we chose the following reaction (entry 5, Table 1 of the main text) as our model system for elucidating the enantio-determining step of the reaction (Scheme S14).

Scheme S14. Model reaction for computational studies.

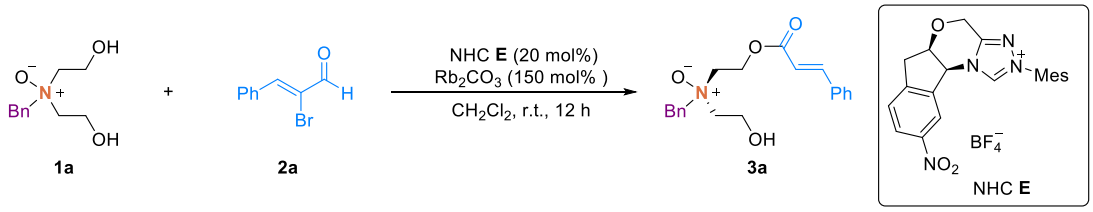

4.2 Conformational sampling

Constrained conformational sampling of the competing transition states was carried out at GFN2-xTB[1–3] level of theory using the CREST program version 2.12 by Grimme and co-workers.[4,5] The conformers and rotamers ensemble was generated using the iterative metadynamics based on genetic z-matrix crossing algorithm (iMTD-GC). Conformers were further optimized at GFN2-xTB level with very tight (*-opt vtight*) optimization. Due to the very large size of the system under consideration, we chose five of the lowest energy conformers from each reaction path to be further optimized at density functional theory (DFT) level and used for the mechanistic studies.

4.3 Density functional theory (DFT) calculations

DFT calculations were carried out using the *Gaussian 16* rev. B.01 program.[6] The global hybrid functional M06-2X[7] with Karlsruhe basis set of double-ζ valence def2-SVP[8,9] for all atoms were employed for all gas-phase optimizations. The M06-2X functional was chosen for the study of present system, as it has been employed in the studies of NHC organocatalysis with good accuracy.[10–15] Single point (SP) corrections were performed using M06-2X functional and def2-TZVP[8] basis set for all atoms. The implicit SMD continuum solvation model[16] was used to account for the solvent effect of dichloromethane solvent that was used in the experimental reactions. Gibbs energies were evaluated at the room temperature (reaction condition), using the entropic quasi-harmonic treatment scheme of Grimme,[11] at a cut off frequency of 100 cm^{-1}. The free energies were further corrected using standard concentration of 1 mol/L, which was used in solvation calculations. Data analysis was carried out using the GoodVibes code version 3.1.1.[17] Gibbs energies evaluated at SMD(dichloromethane)-

M06-2X/def2-TZVP//M06-2X/def2-SVP level of theory are given in kcal mol^{-1} and used for discussion throughout.

Non-covalent interactions (NCIs) were analyzed using NCIPLOT[18] calculations. The *.wfn* files for NCIPLOT were generated at M06-2X/def2-SVP level of theory. NCI indices calculated with NCIPLOT were visualized at a gradient isosurface value of *s = 0.5* au. These are colored according to the sign of the second eigenvalue (λ_2) of the Laplacian of the density ($\nabla^2\rho$) over the range of –0.1 (purple = attractive) to +0.1 (red = repulsive). Molecular orbitals are visualized using an isosurface value of 0.05 au throughout. All molecular structures and molecular orbitals were visualized using *PyMOL* software.[19]

4.4 Dimer stability of remote diol

We performed DFT calculations to discern the thermodynamics of the dimer complex formation of the remote diol. We found that this dimerization is exergonic, with a Gibbs energy of formation, ΔG_r = –16.9 kcal/mol, consistent with the reported value in literature[20]. In dichloromethane solvent (reaction condition), the Gibbs energy of formation is –1.7 kcal/mol such that the dimer complex formation is favored thermodynamically. As a result, we use the dimer in modelling the reaction mechanism.

Scheme S15. Dimerization of remote diol.

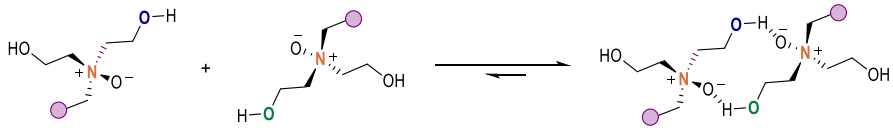

4.5 Enantio-determining transition states for the model system

In the enantio-determining step where the OH group of the remote diol attacks carbonyl carbon of the acyl azolium intermediate (Scheme S13), the nucleophilic O atom can attack from either the *Re* or the *Si* face. Therefore, for each pathway leading to major and minor product, we considered both possibilities of *Re*-face vs *Si*-face attack. As discussed from the computational methods, for each possibility, we performed thorough conformational sampling at xTB level followed by DFT optimization of 5 lowest xTB energy TS conformers. We note that some of these xTB-optimized TS conformers converge to the same TS structure upon DFT optimization.

Figure S15 shows the DFT-optimized lowest energy TS conformer for each possibility. As we can see, for the pathway leading to the major product, the *Re*-face attack by hydroxy oxygen of the diol dimer via **TS_major_Re** ($\Delta\Delta G^{\ddagger}$ = 0.0 kcal/mol) has a lower barrier than the *Si*-face attack by hydroxy oxygen of the diol dimer via **TS_major_Si**

($\Delta\Delta G^{\ddagger}$ = 2.6 kcal/mol) by 2.6 kcal/mol. On the other hand, for the pathway leading to the minor product, the *Si*-face attack by hydroxy oxygen of the diol dimer via **TS_minor_Si** ($\Delta\Delta G^{\ddagger}$ = 1.1 kcal/mol) has a lower barrier than the *Re*-face attack by hydroxy oxygen of the diol dimer via **TS_minor_Re** ($\Delta\Delta G^{\ddagger}$ = 5.3 kcal/mol) by 4.2 kcal/mol. Thus, for the reaction pathway leading to the major product, the diol dimer is likely to attack the acyl azolium intermediate from the *Re*-face via **TS_major_Re** whereas for the pathway leading to the minor product, the diol dimer is likely to attack the acyl azolium intermediate from the *Si*-face attack via **TS_minor_Si**. The energy barrier difference, $\Delta\Delta G^{\ddagger}$ = 1.1 kcal/mol, translates to an enantiomeric ratio of 86:14, in excellent agreement with the observed experimental enantiomeric ratio of 85:15.

TS_major_Re	**TS_major_Si**
$\Delta\Delta G^{\ddagger}$ = 0.0 kcal/mol	$\Delta\Delta G^{\ddagger}$ = 2.6 kcal/mol
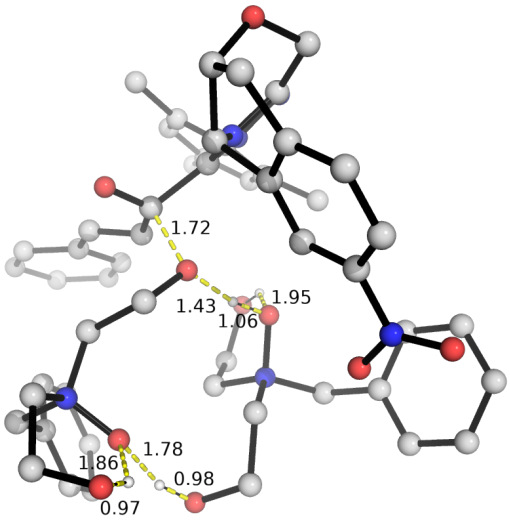	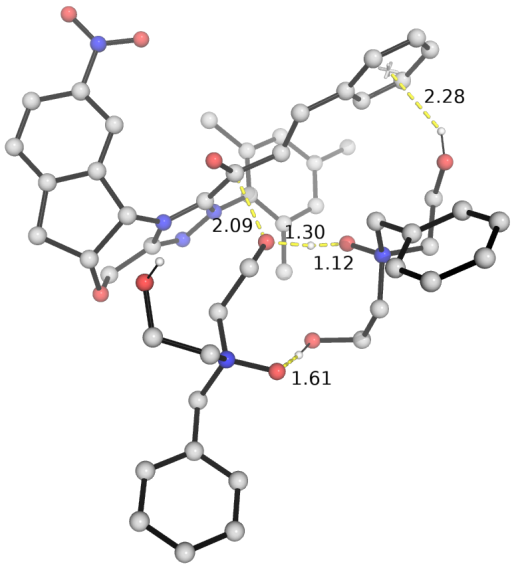
TS_minor_Re	**TS_minor_Si**
$\Delta\Delta G^{\ddagger}$ = 5.3 kcal/mol	$\Delta\Delta G^{\ddagger}$ = 1.1 kcal/mol

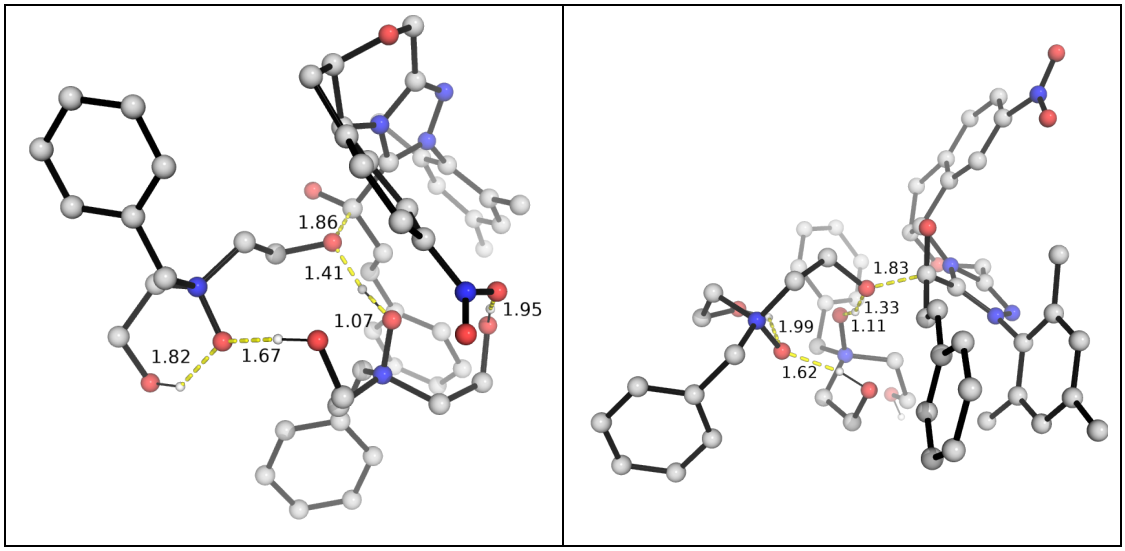

Figure S15. DFT-optimized structures of the enantio-determining transition state structures. Non-polar H atoms are hidden for clarity. Bond distances are given in Å.

To further analyze the molecular origins giving rise to the observed enantioselectivity, we plotted the frontier molecular orbitals as well as the non-covalent interactions (NCIs) in the lowest energy TS for each of the major (**TS_major_Re**) and minor (**TS_minor_Si**) pathway, as shown in Figure S16. We observed that the HOMOs in both **TS_major_Re** and **TS_minor_Si** have similar structure, with dominant orbital coefficient on the styrene motif of the acyl azolium intermediate. Similarly, the LUMOs in both TSs are similar, with dominant orbital coefficient on the carbene motif. For non-covalent interactions, **TS_major_Re** seems to have qualitatively more attractive interactions (purple in color) than those present in **TS_minor_Si**, thus accounting for its slightly lower activation barrier.

	TS_major_Re	**TS_minor_Si**
ΔΔG‡	0.0 kcal/mol	1.1 kcal/mol
DFT structure	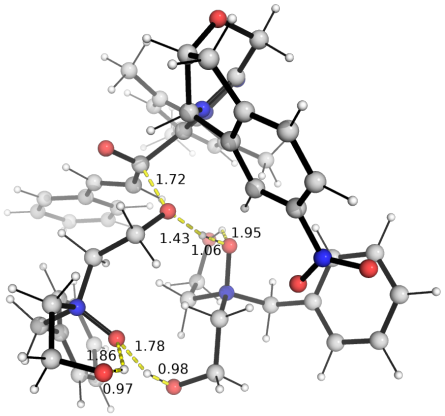	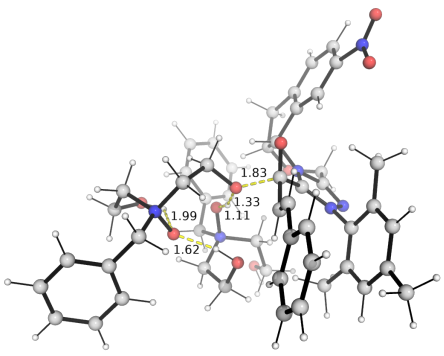

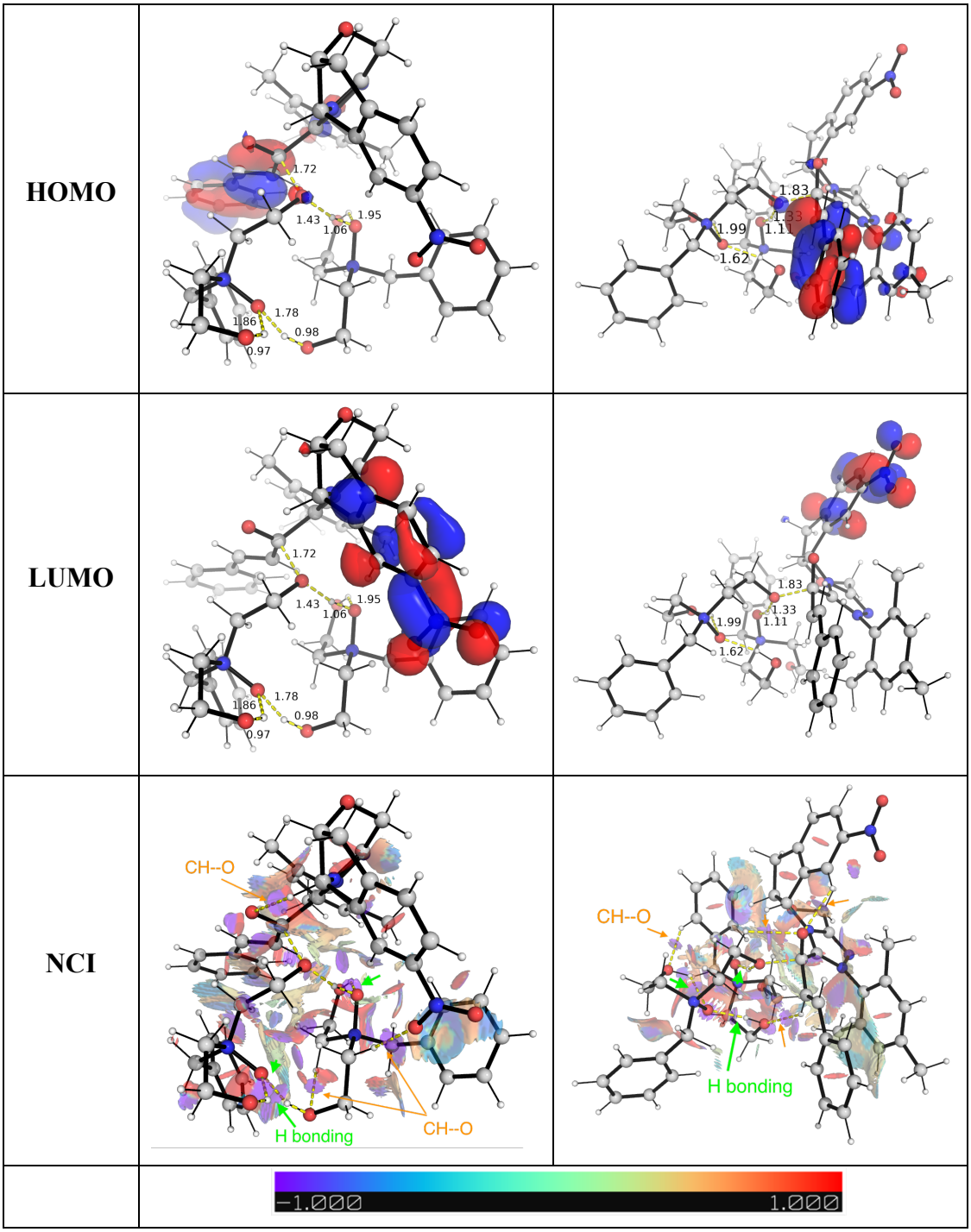

Figure S16. DFT-optimized structures of the enantio-determining transition state structures. Bond distances are given in Å.

4.6 Enantio-determining transition states for the full system

For the real system, instead of mesityl group used in the carbene, the carbene has the 2,4,6-(^{i}Pr$_3$)C$_6$H$_2$ group. As the Mes-group lies away from the center where the C–O bond formation takes place (see DFT optimized structures, Figure S12), we anticipate that it will have a marginal influence on the bond formation event and that our results

from the model system may be satisfactorily extrapolated to the real system: the TS leading to the major product will be favored over the TS leading to the minor product due to more favorable non-covalent interactions present in the former than the latter. The additive chiral phosphoric acid **C-3** is likely to reinforce this trend such that the enantioselectivity is much augmented in favor of the major product.

Scheme S16. Full system for computational studies.

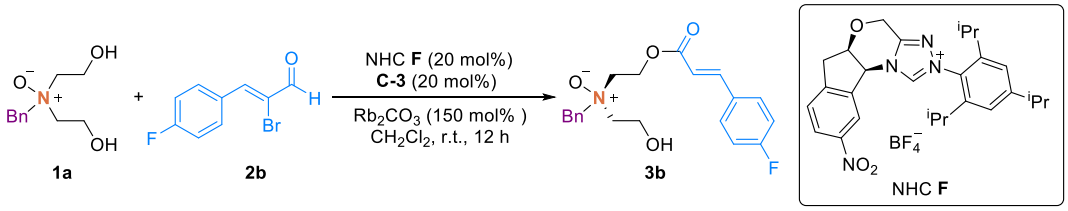

To ascertain the effect of chiral phosphoric acid **C-3**, we study the full system shown in Scheme S16. Due to the very large system size (258 atoms), we endeavored to study the enantio-determining step in a simplified way. We modified the lowest competing TSs (**TS_major_R** and **TS_minor_Si**) from the model system to the full system and add in chiral phosphoric acid **C-3**. Note that **C-3** was added in a random position where its distance to the model system is high (> 2Å). We then restrained the core region where the bond forming event takes place with a force constant of 0.5 a.u. and run CREST conformational sampling to sample all possible conformers in which **C-3** can interact with acyl azolium-dimer complex. The lowest conformer from major and minor pathways are then taken without further geometry optimization and single point energy calculations in solvent phase on these xTB-optimized structures were performed.

	TS_major_Re_full	**TS_minor_Si_full**
ΔΔE‡	0.0 kcal/mol	1.7 kcal/mol
GFN2-xTB structure	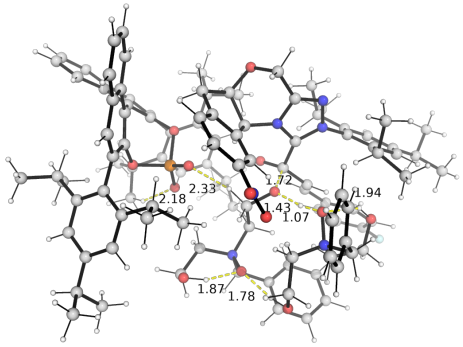	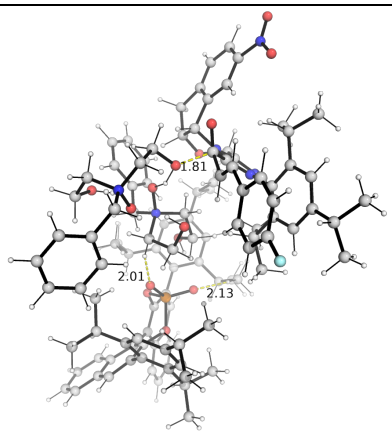

Figure S17. GFN2-xTB-optimized structures of the enantio-determining transition state structures for the full system shown in Scheme S16. Note that the reaction

center/core region are the same as DFT optimized structures in Figure S17, as there were constrained in CREST sampling. Bond distances are given in Å.

The structures and relative energy differences are shown in Figure S13. Using this simplified computational method as an approximation, we found that, for the full system, the TS giving the major product has a barrier that is 1.7 kcal/mol lower than the TS giving the minor product. This confirms our postulate that the additive chiral phosphoric acid **C-3** enhances the favorable interactions in the TS leading to the major more than in the TS leading to the minro product (c.f., in the model system this barrier difference, $\Delta\Delta G^{\ddagger}$, is 1.1 kcal/mol). This $\Delta\Delta E^{\ddagger}$ of 1.7 kcal/mol translates to an enantiomeric excess of 89.3% corresponding to an enantiomeric ratio of 95:5, consistent with the observed experimental enantiomeric ratio, which also happens to be 95:5.

4.7 Optimized structures and raw energy values

Geometries of all optimized structures (in .xyz format with their associated gas-phase energy in Hartrees) are included in a separate folder named *DFT_optimized_structures* with an associated readme.txt file. All these data have been uploaded to zenodo.org (https://zenodo.org/record/10992928).

Absolute values (in Hartrees) for SCF energy, zero-point vibrational energy (ZPE), enthalpy and quasi-harmonic Gibbs free energy for M06-2X/def2-SVP optimized structures and single point corrections in SMD(dichloromethane) using M06-2X/def2-TZVP functional are also included.

Structures	E/au	ZPE/au	H/au	T.S/au	qh-G/au	SP SMD(CH_2Cl_2) M06-2X/def2-TZVP
1a	-708.884679	0.277357	-708.5917	0.054451	-708.644364	-709.731607
1a_dimer	-1417.821643	0.558614	-1417.2322	0.089485	-1417.315698	-1419.491224
TS_major_Re	-3095.002582	1.085203	-3093.8547	0.156536	-3093.997974	-3098.578969

TS_major_Re_c2	-3094.998388	1.084224	-3093.8521	0.157762	-3093.994918	-3098.574147
TS_major_Si	-3094.991022	1.082167	-3093.8462	0.159381	-3093.990405	-3098.570913
TS_minor_Re	-3094.998068	1.085011	-3093.8512	0.155528	-3093.993127	-3098.570797
TS_minor_Si	-3095.00556	1.083323	-3093.8603	0.155025	-3094.00222	-3098.576081
TS_minor_Si_c2	-3095.002942	1.08192	-3093.8588	0.156573	-3094.001547	-3098.573637
TS_minor_Si_c3	-3095.004528	1.08312	-3093.8594	0.155586	-3094.001534	-3098.575001

4.8 References for computational section

Full reference for Gaussian software:

Gaussian 16, Revision B.01, Frisch, M. J.; Trucks, G. W.; Schlegel, H. B.; Scuseria, G. E.; Robb, M. A.; Cheeseman, J. R.; Scalmani, G.; Barone, V.; Mennucci, B.; Petersson, G. A.; Nakatsuji, H.; Caricato, M.; Li, X.; Hratchian, H. P.; Izmaylov, A. F.; Bloino, J.; Zheng, G.; Sonnenberg, J. L.; Hada, M.; Ehara, M.; Toyota, K.; Fukuda, R.; Hasegawa, J.; Ishida, M.; Nakajima, T.; Honda, Y.; Kitao, O.; Nakai, H.; Vreven, T.; Montgomery Jr., J. A.; Peralta, J. E.; Ogliaro, F.; Bearpark, M.; Heyd, J. J.; Brothers, E.; Kudin, K. N.; Staroverov, V. N.; Kobayashi, R.; Normand, J.; Raghavachari, K.; Rendell, A.; Burant, J. C.; Iyengar, S. S.; Tomasi, J.; Cossi, M.; Rega, N.; Millam, J. M.; Klene, M.; Knox, J. E.; Cross, J. B.; Bakken, V.; Adamo, C.; Jaramillo, J.; Gomperts, R.; Stratmann, R. E.; Yazyev, O.; Austin, A. J.; Cammi, R.; Pomelli, C.; Ochterski, J. W.; Martin, R. L.; Morokuma, K.; Zakrzewski, V. G.; Voth, G. A.; Salvador, P.; Dannenberg, J. J.; Dapprich, S.; Daniels, A. D.; Farkas, Ö.; Foresman, J. B.; Ortiz, J. V; Cioslowski, J.; Fox, D. J. Gaussian, Inc., Wallingford CT, 2016.

1. C. Bannwarth, S. Ehlert, S. Grimme, GFN2-xTB - An Accurate and Broadly Parametrized Self-Consistent Tight-Binding Quantum Chemical Method with Multipole Electrostatics and Density-Dependent Dispersion Contributions. *J. Chem. Theory Comput.* **2019**, *15*, 1652.
2. S. Grimme, C. Bannwarth, P. Shushkov, A Robust and Accurate Tight-Binding

Quantum Chemical Method for Structures, Vibrational Frequencies, and Noncovalent Interactions of Large Molecular Systems Parametrized for All spd-Block Elements (Z = 1-86). *J. Chem. Theory Comput.* **2017**, *13*, 1989.

3. C. Bannwarth, E. Caldeweyher, S. Ehlert, A. Hansen, P. Pracht, J. Seibert, S. Spicher, S. Grimme, Extended tight-binding quantum chemistry methods. *Wiley Interdiscip. Rev. Comput. Mol. Sci.* **2021**, *11*, e1493.
4. S. Grimme, Exploration of Chemical Compound, Conformer, and Reaction Space with Meta-Dynamics Simulations Based on Tight-Binding Quantum Chemical Calculations. *J. Chem. Theory Comput.* **2019**, *15*, 2847.
5. P. Pracht, F. Bohle, S. Grimme, Automated exploration of the low-energy chemical space with fast quantum chemical methods. *Phys. Chem. Chem. Phys.* **2020**, *22*, 7169.
6. M. J. Frisch, G. W. Trucks, H. B. Schlegel, G. E. Scuseria, M. A. Robb, J. R. Cheeseman, G. Scalmani, V. Barone, G. A. Petersson, H. Nakatsuji, X.Li, M. Caricato, A. V. Marenich, J. Bloino, B. G. Janesko, R. Gomperts, B. Mennucci, D. J. Hratch, Gaussian 16, Revision B.01, **2016**.
7. Y. Zhao, D. G. Truhlar, The M06 suite of density functionals for main group thermochemistry, thermochemical kinetics, noncovalent interactions, excited states, and transition elements: two new functionals and systematic testing of four M06-class functionals and 12 other function. *Theor. Chem. Acc.* **2008**, *120*, 215.
8. F. Weigend, R. Ahlrichs, Balanced basis sets of split valence, triple zeta valence and quadruple zeta valence quality for H to Rn: Design and assessment of accuracy. *Phys. Chem. Chem. Phys.* **2005**, *7*, 3297.
9. F. Weigend, Accurate Coulomb-fitting basis sets for H to Rn. *Phys. Chem. Chem. Phys.* **2006**, *8*, 1057.
10. X. Yang, Y. Xie, J. Xu, S. Ren, B. Mondal, L. Zhou, W. Tian, X. Zhang, L. Hao, Z. Jin, Y. R. Chi, Carbene-Catalyzed Activation of Remote Nitrogen Atoms of (Benz)imidazole-Derived Aldimines for Enantioselective Synthesis of Heterocycles. *Angew. Chem. Int. Ed.* **2021**, *60*14, 7906.
11. R. Song, Y. Liu, P. K. Majhi, P. R. Ng, L. Hao, J. Xu, W. Tian, L. Zhang, H. Liu, X. Zhang, Y. R. Chi, Enantioselective modification of sulfonamides and sulfonamide-containing drugs: Via carbene organic catalysis. *Org. Chem. Front.* **2021**, *8*, 2413.

12. Y. Lv, G. Luo, Q. Liu, Z. Jin, X. Zhang, Y. R. Chi, Catalytic atroposelective synthesis of axially chiral benzonitriles via chirality control during bond dissociation and CN group formation. *Nat. Commun.*, **2022**, ***13***, 1.
13. R. Deng, S. Wu, C. Mou, J. Liu, P. Zheng, X. Zhang, Y. R. Chi, Carbene-Catalyzed Enantioselective Sulfonylation of Enone Aryl Aldehydes: A New Mode of Breslow Intermediate Oxidation. *J. Am. Chem. Soc.*, **2022**, 144, 5441.
14. W. X. Lv, H. Chen, X. Zhang, C. C. Ho, Y. Liu, S. Wu, H. Wang, Z. Jin, Y. R. Chi, Programmable selective acylation of saccharides mediated by carbene and boronic acid. *Chem*. **2022**, *8*, 1518.
15. X. Yang, L. Wei, Y. Wu, L. Zhou, X. Zhang, Y. R. Chi, Atroposelective Access to 1,3-Oxazepine-Containing Bridged Biaryls via Carbene-Catalyzed Desymmetrization of Imines. *Angew. Chem. Int. Ed.*, **2022**, *62*, e202211977.
16. A. V. Marenich, C. J. Cramer, D. G. Truhlar, Universal solvation model based on solute electron density and on a continuum model of the solvent defined by the bulk dielectric constant and atomic surface tensions. *J. Phys. Chem. B*, **2009**, *113*, 6378.
17. G. Luchini, J. V Alegre-Requena, I. Funes-Ardoiz, R. S. Paton, R. Pollice, GoodVibes: automated thermochemistry for heterogeneous computational chemistry data. **2020**, *9*, 291.
18. J. Contreras-García, E. R. Johnson, S. Keinan, R. Chaudret, J. P. Piquemal, D. N. Beratan, W. Yang, NCIPLOT: A program for plotting noncovalent interaction regions. *J. Chem. Theory Comput.*, **2011**, *7*, 625.
19. L. Schrödinger, The PyMOL Molecular Graphics Development Component, Version 1.8. **2015**.
20. M. Meot-Ner, The ionic hydrogen bond. *Chem. Rev.* **2005**, *105*, 213.